The International Journal of Advanced Manufacturing Technology (2021) 117:2715–2726
https://doi.org/10.1007/s00170-021-07868-9

ORIGINAL ARTICLE

Integration of tube end forming in wire arc additive manufacturing: An experimental and numerical investigation

João PM Pragana[1] · Ivo MF Bragança[2] · Carlos MA Silva[1] · Paulo AF Martins[1]

Received: 12 May 2021 / Accepted: 9 August 2021 / Published online: 16 August 2021

Abstract

Integration of tube end forming operations in metal additive manufacturing routes has a great potential for the fabrication of customized features in additively deposited hollow parts. This paper is focused on the integration of tube expansion with rigid tapered conical mandrels to highlight the advantages in the construction of overhanging flares derived from the elimination of support structures and prevention of humping. The work draws from the mechanical and formability characterization of stainless steel AISI 316L tubes produced by wire arc additive manufacturing (WAAM) to the experimental and numerical simulation of the construction of overhanging flares by tube expansion. Strain loading paths obtained from digital image correlation and finite element analysis combined with the strain values at the onset of necking and fracture allow determining the critical ductile damage that additively deposited tubes can safely withstand. Results show that despite formability of additively deposited tubes being influenced by a dendritic based microstructure, their performance is adequate for tube end forming operations, such as tube expansion, to be successfully integrated in metal additive manufacturing without the need of using expensive hardware and complex deposition strategies.

Keywords Hybrid manufacturing · Tube forming · Wire arc additive manufacture · Experimentation · Finite element method · Formability

1 Introduction

In recent years, the capabilities of metal additive manufacturing (MAM) for operating beyond the boundaries of conventional manufacturing have been the subject of intense research [1, 2]. MAM is nowadays seen as an effective option to fabricate highly customized parts with sophisticated shapes and/or tailored features that are difficult or even impossible to be economically produced through conventional manufacturing [3].

✉ Paulo AF Martins
pmartins@tecnico.ulisboa.pt

João PM Pragana
joao.pragana@tecnico.ulisboa.pt

Ivo MF Bragança
ibraganca@dem.isel.ipl.pt

Carlos MA Silva
carlos.alves.silva@tecnico.ulisboa.pt

[1] IDMEC, Instituto Superior Técnico, Universidade de Lisboa, Lisbon, Portugal

[2] CIMOSM, Instituto Superior de Engenharia de Lisboa, Instituto Politécnico de Lisboa, Lisbon, Portugal

The most widespread MAM processes are usually classified into two distinct categories: (i) powder bed fusion (PBF) and (ii) direct energy deposition (DED). In PBF, parts are built up layer by layer by spreading several beds of metallic powder onto a platform, which are selectively melted and bonded together by means of focused laser [4] or electron beam [5] thermal heat sources. In DED, the feedstock is not spread onto a platform, but fed and melted instantaneously through the combined action of a supply unit and a thermal heat source. Laser, electron beam and electric arc can be used as thermal heat sources [6].

PBF and DED processes have been under continuous development and improvement throughout the past years to achieve levels of applicability and flexibility that are nowadays appropriate to fabricate high-quality near net-shape parts for many different industries [7]. The progress made in the last two decades is remarkable, but the fabrication of complex parts by metal deposition in successive layers is still difficult and limited by the intrinsic characteristics of the processes.

In the case of PBF processes, for example, the fabrication of parts with complex-shaped features cannot avoid using support structures, as it is schematically shown in the left side of Fig. 1a. These structures, which are crucial for preserving

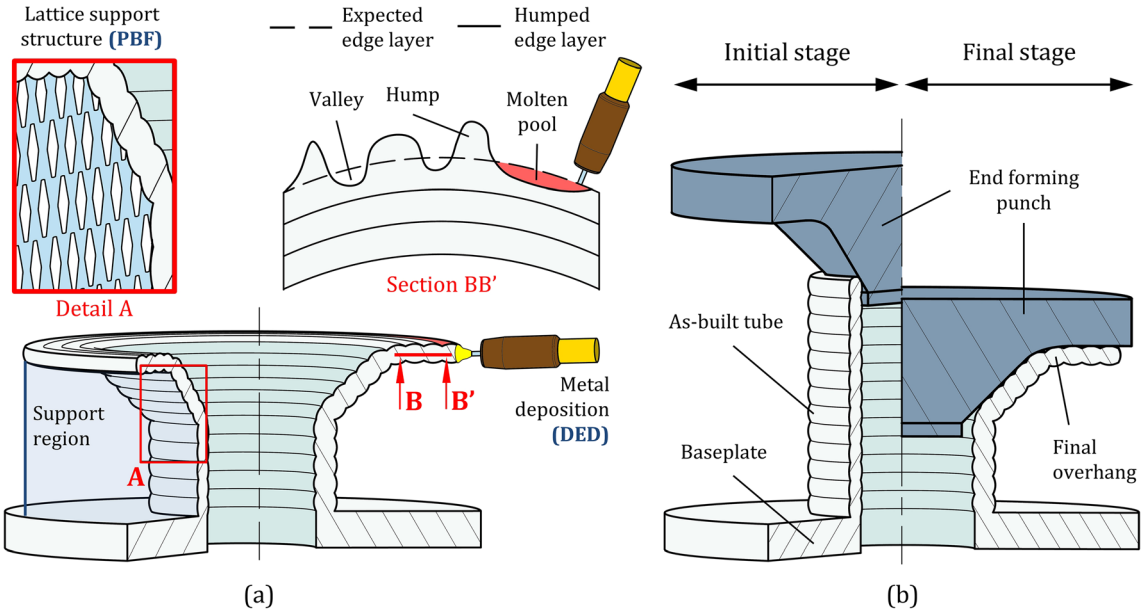

Fig. 1 **a** Schematic representation of the construction of overhanging flares in axisymmetric hollow parts using (left) PBF with details of the supports and (right) DED with details of the humps. **b** The new proposed hybrid metal additive manufacturing (HMAM) approach based on the integration of tube expansion in metal additive manufacturing (MAM)

the overall geometric integrity of the parts and preventing the occurrence of defects and failures such as deformations, dross formation or warpage, must be removed after finishing material deposition. The problem is that post-processing operations to eliminate support structures are time- and energy-consuming and may, in some cases, not fully achieve the desired objectives [8].

In the case of DED, recent published work shows that the use of support structures in parts with overhang features or hollow sections can be avoided by using deposition strategies based on multi-directional paths that are carried out in robots with multiple degrees of freedom [9]. However, this requires difficult programming and expensive hardware and can be complicated to accomplish when the parts are large or complex-shaped [10]. Moreover, even the most sophisticated deposition strategies are limited by an inclination threshold of the thermal heat source above which the deposited material layers will give rise to irregular shapes with severe undulations (commonly designated as 'humps') [11].

Humping (right side of Fig. 1a) is a well-known defect in down hand fusion welding processes, and its occurrence can be minimized by reducing the travel speed of the heat source [10]. However, the implementation of such a solution in DED is not feasible because it would inevitably lead to a reduction in the material deposition rate and to a worsening of the already low productivity of these processes when compared to conventional manufacturing [12].

The main conclusion to be derived from the above-mentioned drawbacks of MAM and from its intrinsic limitations associated to high energy requirements, lack of precision and poor surface quality of the deposited parts is the need to develop new and more effective deposition strategies through integration of conventional manufacturing in additive manufacturing routes. Hybridization of additive manufacturing by integration of metal cutting operations at the end of material deposition is a good example of a well-established solution for fabricating parts with significant gains in quality and productivity [13]. In fact, several commercial hybrid additive manufacturing systems based on this approach are available in the market since the earliest 2010s [14].

However, what this paper aims to explore is not the hybridization of additive manufacturing by integration of metal cutting operations but the hybridization of additive manufacturing by integration of metal forming operations to increase its overall sustainability and to reduce its dependence on the batch size [15, 16]. Several feasibility studies have been recently published on the integration of sheet metal forming [17–20] and bulk metal forming [21–24] with additive manufacturing. The state-of-the-art review by Pragana et al. [25] presents and discusses the major scientific and technological breakthroughs resulting from these studies but also allows concluding that hybridization of additive manufacturing by integration of tube forming operations is an open field of research.

The above conclusion is nonetheless surprising because tube end forming operations such as expansion, reduction, flaring and inversion [26] have a great potential to fabricate customized features in additively deposited hollow parts in small production lead times. Referring, for example, to Fig. 1b, it follows that hybridization of additive manufacturing with tube expansion facilitates the construction of overhanging flares in rotationally symmetric hollow parts because it

eliminates the need of support structures and prevents the formation of humps.

Under these circumstances, the main objective of this paper is to investigate the feasibility of integrating tube expansion with a rigid tapered conical mandrel in additive manufacturing routes. For this purpose, authors carried out a numerical and experimental investigation aimed at characterizing the strain loading paths and the in-plane strains at the onset of necking and fracture during the expansion of wire arc additively manufactured tubes. Results are compared against the formability limits that were previously determined by means of tension and ring hoop tension tests and against those obtained for commercial wrought tubes, which are included for reference purposes. Results show that despite formability of deposited tubes being influenced by a dendritic based microstructure, their capability of withstanding large plastic deformations without failure is adequate for the successful integration of tube expansion in metal additive manufacturing of complex hollow parts without resorting to expensive hardware and complex deposition strategies.

2 Materials and methods

2.1 Additively deposited and wrought commercial tubes

The investigation was carried out in stainless steel AISI 316L tubes deposited by wire arc additive manufacturing (WAAM) in a 3-axis CNC system equipped with a ESAB LUC Aristo 400 gas metal arc welding machine. The material was supplied as a wire with 1-mm diameter through a welding torch and melted, at the time of deposition, onto tubular preforms with approximately 42 mm of outer diameter and 5 mm of wall thickness (Fig. 2a). Deposition was carried out one layer at a time with a single bead in a criss-cross sequence for evenly distributing the heating-cooling cycles and to avoid concentrating the overlapped beads along the same planar coordinates of the preform. The shielding gas was 99.9% of argon, and the main parameters utilized in the deposition are summarized in Table 1.

After deposition, tubes with an outer radius $r_0 = 20$ mm, a wall thickness $t_0 = 1.5$ mm and a total length $l_0 = 70$ mm were machined from the additively manufactured tubular preforms by turning (Fig. 2b). Turning was performed with a cutting speed of 150 m/min, a feed of 0.15 mm/rev and a depth of cut of 0.25 mm. The goal was to obtain tubes with dimensions and surface quality (average roughness $R_a = 0.75$ μm) like those of the wrought commercial stainless steel AISI 316L tubes that were used for reference purposes. However, in typical hybrid metal additive manufacturing routes resulting from the integration of tube end forming with additive manufacturing, there will be no intermediate machining operations unless strictly necessary.

2.2 Flow curve and formability limits of the tubes

In a recent work, authors performed the mechanical and formability characterization of the additively manufactured and commercial wrought stainless steel AISI 316L tubes [27]. The flow curves and the anisotropy coefficients were directly obtained from conventional tension tests (TTs) in specimens that were machined out from the longitudinal (L) tube direction and from ring hoop compression tests (RHTTs) in specimens that were machined out from the transverse (T) (i.e. circumferential) and 45° inclined (I) directions.

The TTs were performed in accordance with the ASTM standards E8/E8M [28], whereas the RHTTs followed the guidelines of the ASTM standards D2290-00 [29] applicable to plastic or reinforced plastic tubes, which recommend the use of two dumbbell geometries located 180° degrees apart. The results of the tests are summarized in Fig. 3 and Table 2.

The formability limits of the tubes at the onset of necking and fracture were obtained by means of digital image correlation (DIC) and by measuring the thickness along the cracks at the end of the tests. Details of the overall procedure are given in Pragana et al. [27], and the fracture forming limit (FFL) line resulting from this previous work will be utilized in the forthcoming sections of this paper dealing with the formability of the additively manufactured tubes in expansion.

2.3 Tube expansion tests

The tube expansion tests were carried out at ambient temperature in an Instron SATEC 1200 hydraulic testing machine with a crosshead speed of 5 mm/min. Figure 2c shows a schematic drawing and a photograph of the active tool components that were utilized in the expansion of the commercial wrought and additively manufactured tubes with a rigid tapered conical mandrel. The mandrel had an inclination angle $\varphi = 30°$, and a tubular sleeve was included to prevent local buckling during axial compression. Molybdenum disulphide grease (MoS_2)

Table 1 Wire arc additive manufacturing parameters that were used to fabricate the AISI-316L stainless steel tubular preforms

Current (A)	Voltage (V)	Wire feed speed (m/min)	Travel speed (m/min)	Stick-out length (mm)	Gas flow rate (l/min)	Bead height (mm)
100	16.5	6	0.6	10	10	1.8

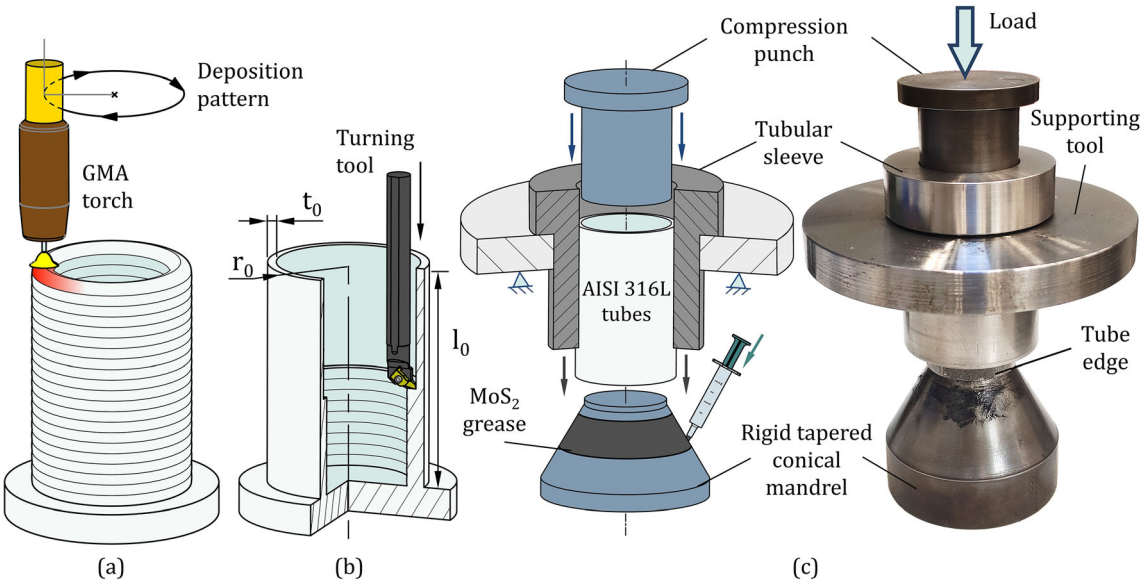

Fig. 2 Schematic representations. **a** Deposition of the AISI 316-L stainless steel tubular preforms. **b** Subsequent machining operation. **c** Expansion with a rigid tapered conical mandrel

was utilized as lubricant on the contact surfaces between the tapered conical mandrel and the inner tube radius.

The outer surface of the tube specimens was painted with a white uniform background colour and sprayed with a stochastic black speckle pattern to allow measuring the evolution of the meridional ε_φ and circumferential ε_θ surface strains by means of digital image correlation (DIC) (Fig. 4a). For this purpose, the surfaces of interest were illuminated with a spotlight, and the strains were automatically measured by means of a commercial DIC system from Dantec Dynamics (model Q-400 3D). The system is equipped with 2 cameras with 6 megapixels of resolution and focal lenses of 50.2 mm with an aperture of f/8. The frequency of image acquisition was set to 20 frames per second, and the correlation algorithm made use of the INSTRA 4D software.

The meridional and circumferential surface strains obtained by DIC were plotted in principal strain space (Fig. 4b) to reveal the strain loading path up to the onset of necking $(\varepsilon_\varphi^{\mathrm{i}}, \varepsilon_\theta^{\mathrm{i}})$ corresponding to failure by plastic instability. The onset of failure by fracture corresponds to the strain pairs $(\varepsilon_\varphi^{\mathrm{f}}, \varepsilon_\theta^{\mathrm{f}})$ of the rectangular solid marker in principal strain space and was obtained from the gauge length strains at the tube edge locations where cracks were triggered. The procedure involved determination of the thickness strain at fracture $\varepsilon_{\mathrm{t}}^{\mathrm{f}}$ by measuring the tube wall thickness before t_0 and after t_{f} cracking (refer to the section AA' in Fig. 4b) with a stereomicroscope Mitutoyo TM-505B:

$$\varepsilon_{\mathrm{t}}^{\mathrm{f}} = ln\frac{t_{\mathrm{f}}}{t_0} \tag{1}$$

The circumferential strain at fracture $\varepsilon_\theta^{\mathrm{f}}$ was then determined assuming material incompressibility and that the onset of necking $(\varepsilon_\varphi^{\mathrm{i}}, \varepsilon_\theta^{\mathrm{i}})$ corresponds to the point in principal strain space where the strain loading path changes towards plane strain $(d\varepsilon_\varphi = 0)$ due to localization of plastic deformation:

$$\varepsilon_\theta^{\mathrm{f}} = -\left(\varepsilon_{\mathrm{t}}^{\mathrm{f}} + \varepsilon_\varphi^{\mathrm{i}}\right) \; with \; \varepsilon_\varphi^{\mathrm{f}} = \varepsilon_\varphi^{\mathrm{i}} \tag{2}$$

Table 2 Yield stresses in the longitudinal (L), transverse (T) and inclined (I) directions

	σ_{YL} (MPa)	σ_{YT} (MPa)	σ_{YI} (MPa)
Commercial wrought tubes	510.1	504.7	477.3
Additively manufactured tubes	421.2	377.5	327.9

2.4 Finite element modelling

The expansion of the commercial wrought and additively manufactured tubes was numerically simulated with the in-house finite element computer program i-form [30]. The program is built upon the flow formulation and employs a control volume approach with velocities u_{i} as the primary unknowns of the following modified weak form of the quasi-static force equilibrium equations to include sliding with friction between objects:

$$\int_V \sigma'_{\mathrm{ij}} \delta D_{\mathrm{ij}} dV + \int_V \sigma_{\mathrm{m}} \delta D_{\mathrm{v}} dV - \int_{S_{\mathrm{t}}} t_{\mathrm{i}} \delta u_{\mathrm{i}} dS + \int_{S_{\mathrm{f}}} \left(\int_0^{|u_{\mathrm{r}}|} \tau_{\mathrm{f}} \delta u_{\mathrm{r}} \right) dS = 0 \tag{3}$$

The main symbols in (3) are the deviatoric Cauchy stress σ'_{ij}, the hydrostatic stress σ_{m}, the rate of deformation D_{ij}, the

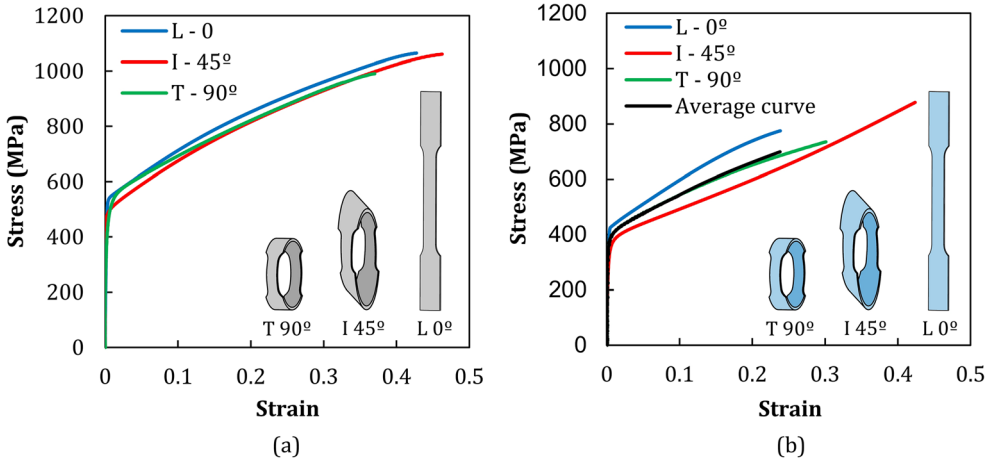

Fig. 3 Flow curves. **a** Commercial wrought AISI 316-L stainless steel tubes. **b** Additively manufactured AISI 316-L stainless steel tubes

volumetric rate of deformation D_v, the tractions t_i applied on the boundary S_t of the control volume and the friction shear stress τ_f and the relative sliding velocity u_r on the contact interfaces S_f between objects.

The constitutive equations relating the deviatoric Cauchy stress σ'_{ij} with the rate of deformation D_{ij} were based on the von Mises isotropic and Hill's 1948 anisotropic yield criteria for the wrought commercial and additively manufactured tubes, respectively.

In the case of the Hill's 1948 plasticity criterion [31],

$$F\left(\sigma_y-\sigma_z\right)^2+G(\sigma_z-\sigma_x)^2+H\left(\sigma_x-\sigma_y\right)^2+2L\tau_{yz}^2+2M\tau_{zx}^2+2N\tau_{xy}^2=\frac{2}{3}(F+G+H)\,\overline{\sigma}^2 \quad (4)$$

the constants F, G, H, L, M, N were determined assuming that $\sigma_{YT}=\sigma_{Yx}=\sigma_{Yy}$ and $\sigma_{YI}=\sigma_{\theta z}=\sigma_{xz}=\sigma_{yz}$ (Fig. 5). These two assumptions considered that the tubes are anisotropic with symmetry in material properties along the transverse (T) direction. This is because different RHTT specimens machined from the transverse (T) direction and having dumbbells in various locations around the perimeter of the tubes were found to provide similar flow curves and yield stress values.

The first of these assumptions was further confirmed by performing stack compression tests in cylindrical test specimens made from three individual discs with 10-mm diameter and 3-mm height. The discs were cut out from the wall thickness of the original tubular preforms by electro-discharge machining in different locations around the tube perimeter (refer to the orthogonal regions I, II, III and IV of Fig. 6a), and the flow curves shown in Fig. 6b confirm that the mechanical response of the additively manufactured AISI 316-L stainless steel tubes is identical along the perimeter.

Combining these two assumptions with the yield stress values in the longitudinal (L), transverse (T) and inclined (I) directions that are given in Table 2, it is possible to obtain the constants of the Hill's 1948 plasticity criterion [31] that are included in Table 3.

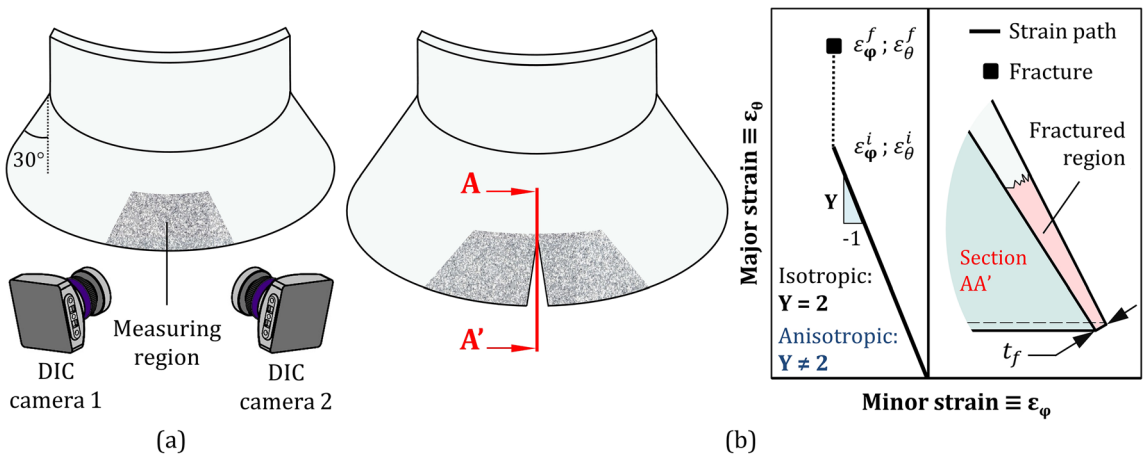

Fig. 4 Schematic representations. **a** Experimental setup utilized by the digital image correlation system. **b** Section AA' along the crack with indication of the tube edge where the wall thickness was measured at the end of tube expansion

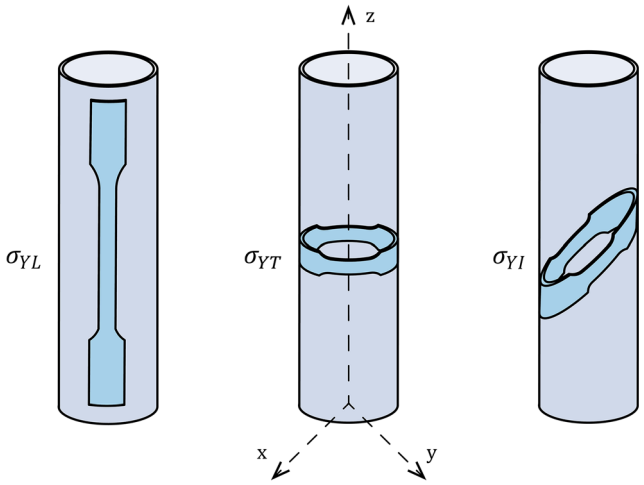

Fig. 5 Representation of the tension and ring hoop test specimens with indication of the *x*, *y*, *z* frame utilized in the finite element modelling of tube expansion

Figure 7 shows a typical finite element model utilized in the numerical simulation of the tube expansion with a rigid tapered conical mandrel. The tubes were discretized with approximately 70,000 hexahedral elements, and the active tool parts (conical mandrel, compression punch and tubular sleeve) were discretized by means of rigid spatial triangular elements.

Friction between the tubes and the active tool parts was modelled with the law of constant friction $\tau_f = mk$, where k is the shear flow stress and m is the friction factor. A value of m equal to 0.1 was applied on the contact surfaces between the tube and the active tool parts after checking the finite element predicted forces that best matched the experimental measurements.

The onset of failure by cracking was modelled by means of the void growth ductile damage-based criterion of McClintock [32], because cracks open by tension (mode I of fracture mechanics) at the tube edges [33].

Table 3 Anisotropy coefficients of the Hill's 1948 plasticity criterion for the wire arc additive manufactured AISI 316L stainless steel tubes

F	*G*	*H*	*L*	*M*	*N*
0.86	0.86	1.28	4.14	4.14	3

Note: *N* was assumed as 3 due to difficulty in obtaining its experimental value in a tube

$$D^{\text{crit}} = \int_0^{\bar{\varepsilon}_f} \frac{\sigma_m}{\bar{\sigma}} d\bar{\varepsilon} \tag{5}$$

Subsequent crack propagation was performed by means of a deletion technique in which elements were removed from the mesh when damage reached a critical value D^{crit}.

The central processing unit (CPU) time for a typical analysis using a convergence criterion for the velocity field and residual force equal to 10^{-3} was approximately 4 h on a computer equipped with an Intel i7-6950X CPU processor.

3 Results and discussion

3.1 Strain loading path

The feasibility of integrating tube expansion in wire arc additive manufacturing (WAAM) routes to prevent the formation of humps, facilitate the construction of overhangs and eliminate the need of support structures requires understanding the

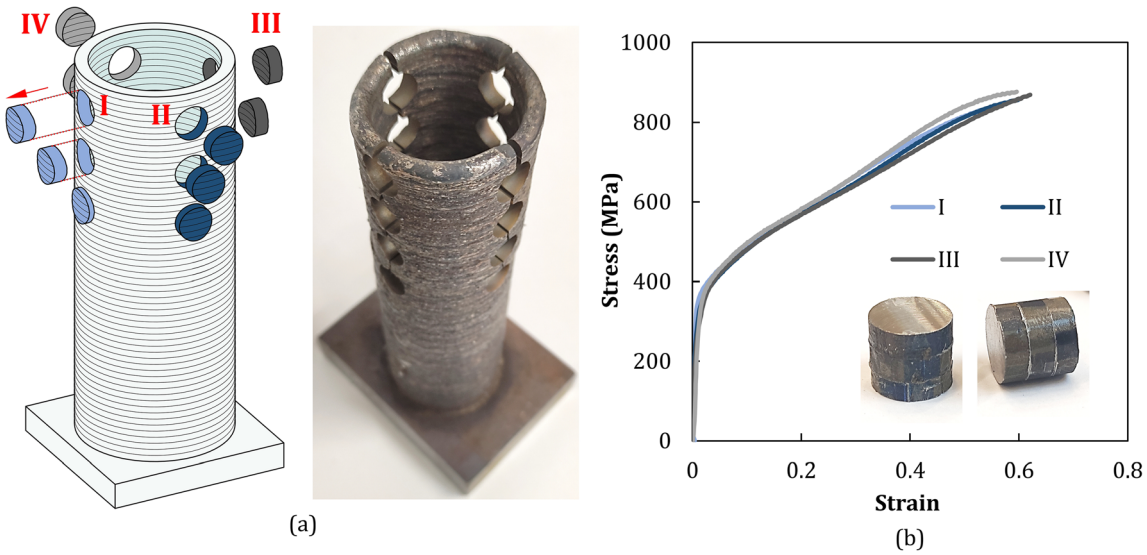

Fig. 6 **a** Schematic representation and photograph of the regions of the tubular preforms from where the cylindrical discs of the test specimens were obtained. **b** Flow curves of the additively manufactured AISI 316-L stainless steel tubes obtained from stack compression tests in the thickness direction

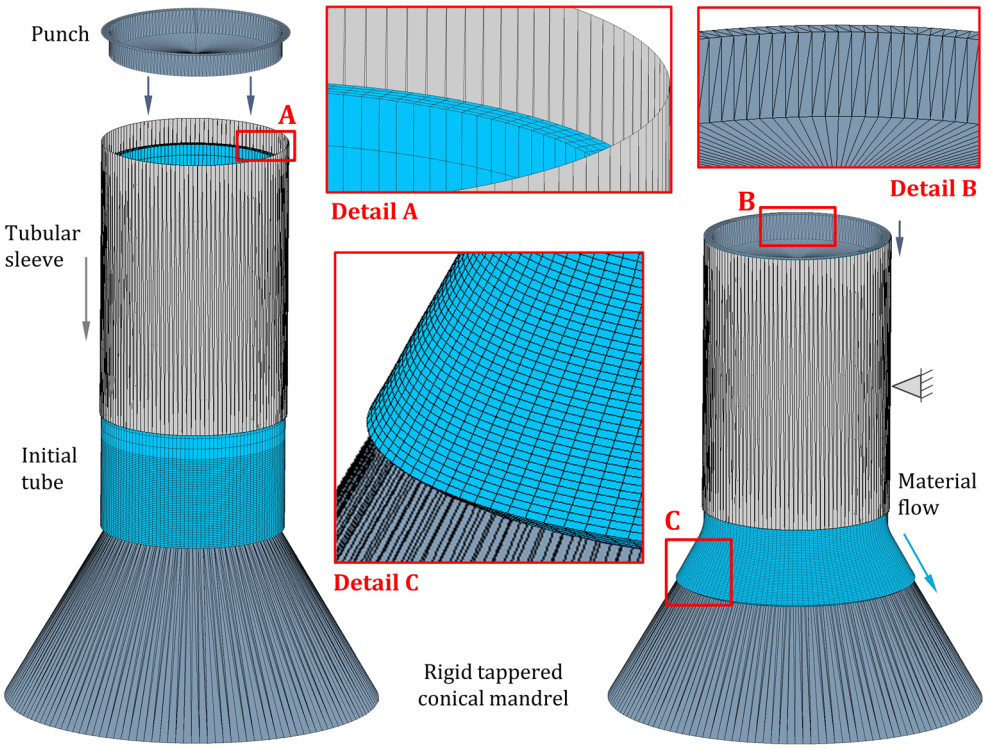

Fig. 7 Typical finite element model utilized in the numerical simulation of tube expansion with a rigid tapered conical mandrel showing details of the tube and of the active tool parts

extent to which the deposited material is ductile enough to withstand the large plastic deformations arising from tube expansion with a rigid tapered conical mandrel.

The solid and dashed blue lines in Fig. 8a are the experimental and finite element predicted strain loading paths for the expansion of the additively manufactured AISI 316L stainless steel tubes with indication of the onset of necking (at the end of the solid and dashed blue lines) and of the onset of fracture (rectangular blue solid marker at the end of the vertical dotted blue line). The results obtained for the wrought commercial AISI 316L stainless steel tubes are depicted in black and are included for reference purposes.

As seen, the strain loading paths of the additively manufactured tubes are slightly deviated towards plane strain due to anisotropy, while those of the wrought commercial tubes, which are isotropic, are in close agreement with uniaxial tension ($d\varepsilon_\theta/d\varepsilon_\varphi = -2$). The anisotropic behaviour of the deposited tubes is caused by a dendritic microstructure that forms in the build direction (longitudinal direction) during the heating and cooling cycles of material deposition (Fig. 8b). The strain values at the onset of failure by fracture are in close agreement with the fracture forming limit (FFL) line that had been previously determined by Pragana et al. [27] using tension tests (TTs) and ring hoop tension tests (RHTTs).

The striations that are visible on the expanded surface of the additively deposited tubes (Fig. 8c) are also related to the dendritic based microstructure and are caused by the growth of stable necks within the primary arms of the dendrites along the circumferential direction subjected to uniaxial tension or near uniaxial tension states of stress. A similar result had already been observed by Pragana et al. [27] in RHTTs performed on specimens machined out from the transverse and inclined directions.

The agreement between the experimental and numerical predicted strain loading paths is very good and confirms that the overall strategy utilized in material characterization and finite element modelling was adequate. Comparison of the local major strain ε_θ values obtained from DIC and finite element modelling that is shown in Fig. 9 further confirms what was said above.

3.2 Damage and cracking

As previously mentioned, the expanded tube edges are subject to uniaxial tension (or near uniaxial tension) in which σ_θ is the only (or the most important) acting stress. The thickness stress $\sigma_t = 0$ and, therefore, the surfaces of the expanded tube edges are regions under plane stress deformation conditions, as may be inferred from the finite element predicted distributions of σ_t that are shown in Fig. 10a.

Taking the above conclusion into consideration, it is possible to transfer the experimental strains obtained by DIC from principal strain space (Fig. 8a) to the space of effective strain $\overline{\varepsilon}$ vs. stress triaxiality $\eta = \sigma_m/\overline{\sigma}$ (Fig. 10b) by means of a simple analytical procedure based on the application of the following two equations derived from Hill's 1948 yield plasticity criterion and associated constitutive equations [34]:

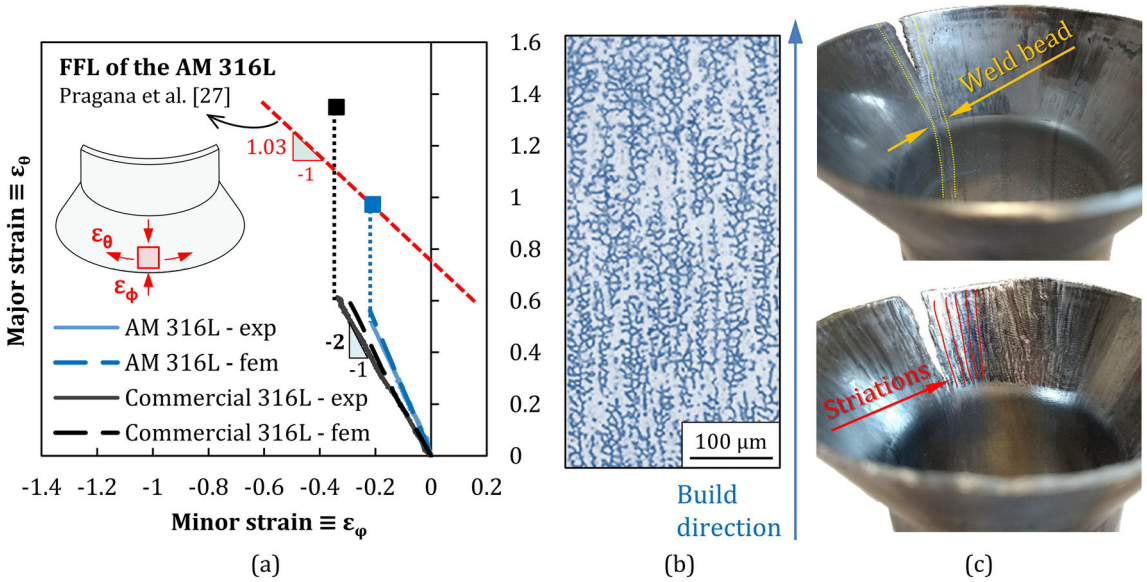

Fig. 8 Tube expansion with a rigid tapered conical mandrel. **a** Experimental and finite element predicted strain loading paths. **b** Dendritic microstructure of the tubes along the build direction. **c** Details of the cracks and of the adjacent surfaces at the end of tube expansion. Note: The rectangular solid markers in (a) are the fracture strains

$$\bar{\varepsilon} = \frac{1+r}{\sqrt{(1+2r)}}\sqrt{\varepsilon_\theta^2 + \varepsilon_\varphi^2 + \frac{2r}{(1+r)}\varepsilon_\theta\varepsilon_\varphi}\frac{\sigma_m}{\sigma} = \frac{1+2r}{3\sqrt{1+2r}}\frac{(1+\beta)}{\sqrt{1+\frac{2r}{1+r}\beta+\beta^2}} \quad (6)$$

In the above equations, the symbol σ denotes the effective stress, σ_m is the hydrostatic (mean) stress, $\beta = d\varepsilon_\theta/d\varepsilon_\varphi$ is the slope of the strain loading path at a specific strain pair (ε_φ, ε_θ), and r is the normal anisotropy taken as 0.7 and 1 for the

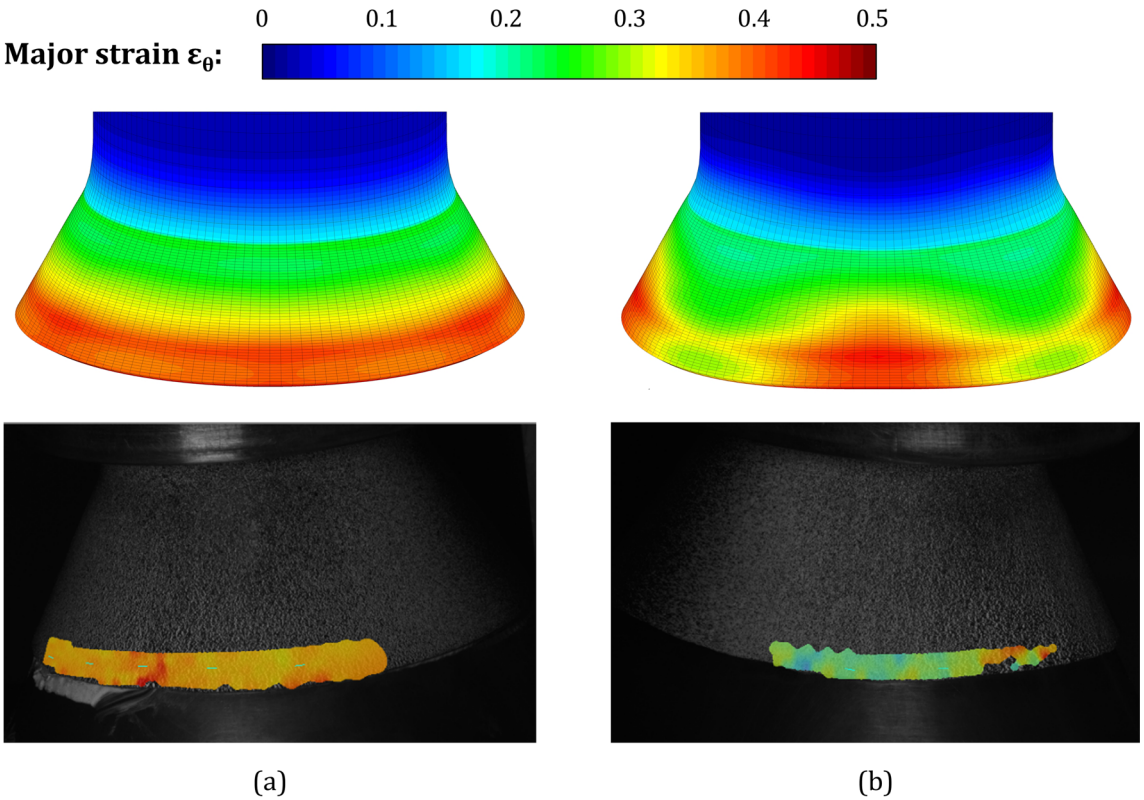

Fig. 9 Finite element and experimental DIC values of the major (circumferential) strain ε_θ for an instant of time close to the onset of failure by necking. **a** Wrought commercial tube. **b** Additively deposited tubes

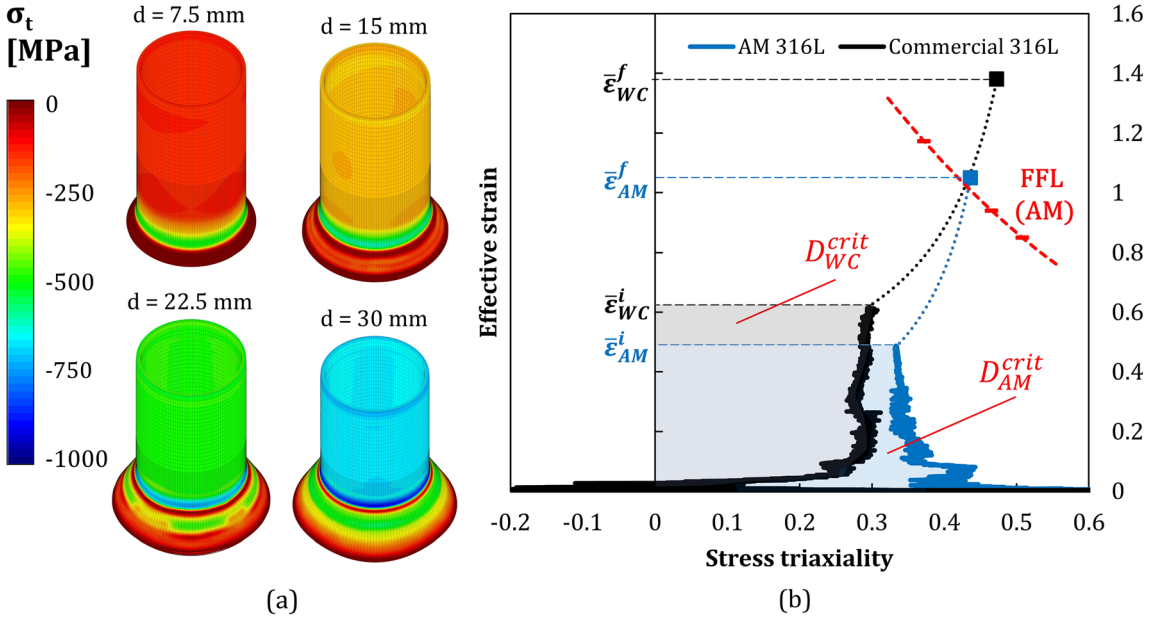

Fig. 10 **a** Finite element predicted distribution of thickness stress σ_t at different instants of tube expansion. **b** Experimental evolution of effective strain with stress triaxiality for the additively manufactured and wrought commercial AISI 316L stainless steel tubes subjected to expansion with a rigid tapered conical mandrel

additively manufactured and wrought commercial AISI 316L stainless steel tubes, respectively [27].

The result of the transference is shown in Fig. 10b, and the two-coloured areas that are bounded by the loading paths and the vertical axis are the experimental critical values D^{crit} (6) of the ductile damage criterion of McClintock [32] for the additively manufactured (AM) and wrought commercial (WC) AISI 316L stainless steel tubes:

$$D_{AM}^{crit} = 0.16 \; ; \; D_{WC}^{crit} = 0.17 \tag{7}$$

As shown in Fig. 10b and Eq. (7), the formability of the wrought commercial tubes is greater than that of the additively manufactured tubes, but the latter are still very much capable of withstanding large plastic deformations and to be successfully integrated in hybrid additive manufacturing routes.

The experimental critical values D^{crit} of ductile damage (7) were utilized in finite element modelling of tube expansion to identify the onset of failure and to perform crack propagation by means of the element deletion technique that was previously described in Sect. 2.3. The result for the additively manufactured tubes is shown in Fig. 11.

3.3 Required forces

Hybridization of additive manufacturing by integration of tube end forming operations such as tube expansion shortens

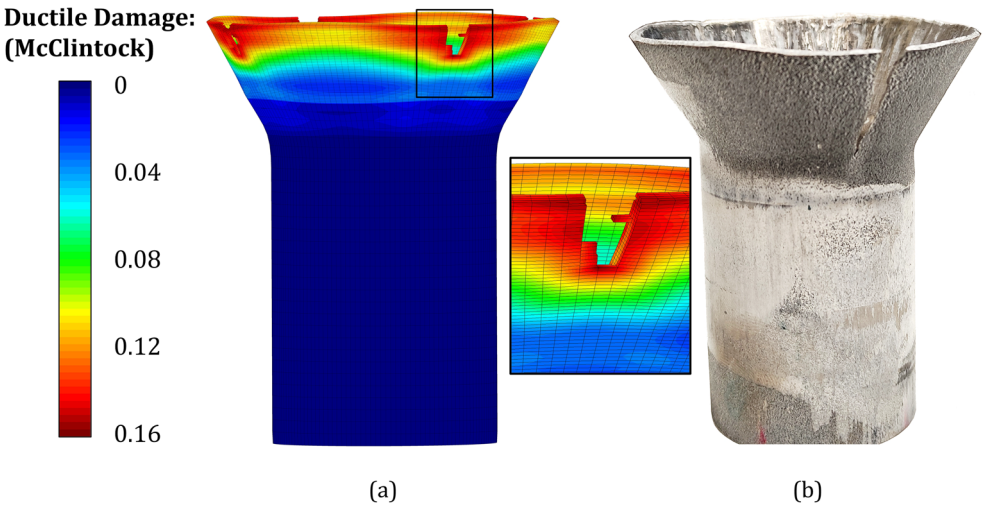

Fig. 11 Finite element predicted distribution of ductile damage according to McClintock [32] criterion after crack initiation and propagation with a photograph of an additively manufactured tube

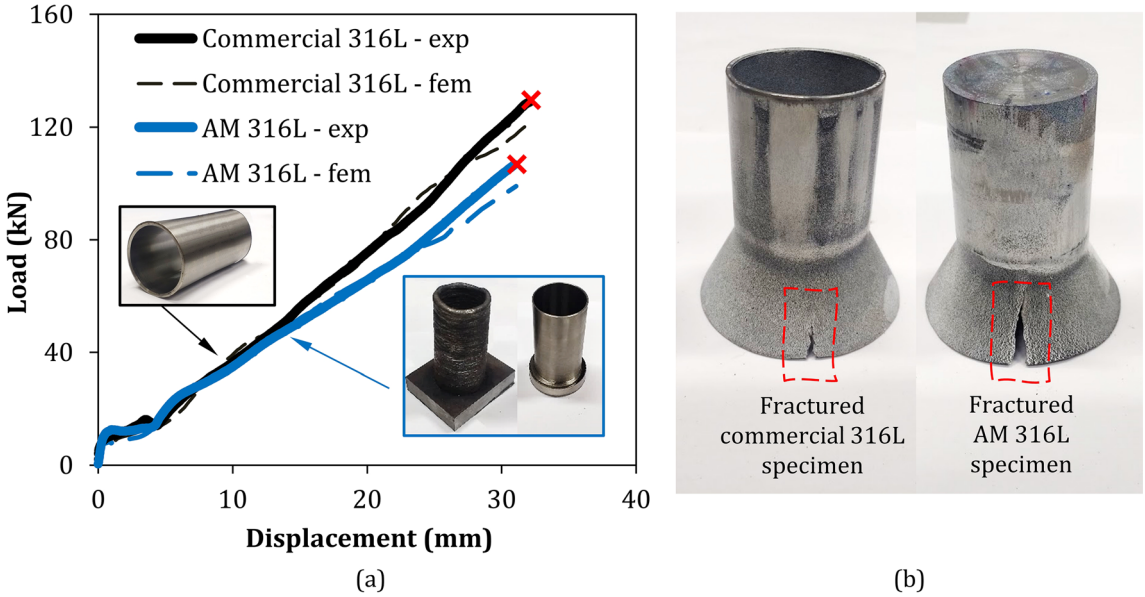

Fig. 12 **a** Experimental and finite element predicted evolution of the force with displacement for the expansion of additively manufactured and wrought commercial AISI316L stainless steel tubes with a rigid tapered conical mandrel. **b** Photographs of the two types of tubes after cracking

the processing time and ensures higher accuracies in the fabrication of complex parts. However, this strategy is dependent on the maximum compression force available in the system, which must be kept as small as possible to avoid removing the parts from the AM system and perform intermediate tube end forming operations in a press.

Finite element simulation is therefore important to predict the required forces and to plan the overall hybrid additive manufacturing route. Figure 12 shows the experimental and finite element predicted evolutions of the force with displacement for the expansion of an additive manufactured AISI 316L stainless steel tube with a rigid tapered conical mandrel.

As seen, the total displacement at the onset of failure is similar, meaning that the expansion of additively manufactured tubes allows constructing overhanging flares with significant diameters of the leading tube edge in rotationally symmetric hollow parts without using support structures or complex deposition strategies. The maximum required force at the instant when the tube fails by necking and subsequent cracking is below 120 kN and roughly 10% smaller than that required by the wrought commercial AISI 316L stainless steel tubes used as a reference. This value is small enough to be easily included in a hybrid additive manufacturing commercial system.

4 Conclusions

Hybridization of metal additive manufacturing by integration of tube end forming operations is feasible because the additive manufactured tubes are capable of withstanding large plastic deformations before failing by necking and subsequent cracking. Experimental and numerical simulation work performed in the expansion of additively manufactured AISI 316L stainless steel tubes with a tapered conical mandrel shows that the overall formability limits by necking and fracture are 21% and 30% smaller than those of wrought commercial tubes due to a dendritic microstructure that forms in the build direction during the heating and cooling cycles of material deposition. However, the additively manufactured tubes are still appropriate to create flares and other overhanging geometries by expansion without resorting to material deposition and to the utilization of additional support structures.

Finite element modelling of tube end forming operations performed with additively manufactured tubes must consider the anisotropic behaviour of the deposited material and is suitable to replicate the strain loading paths and the required forming forces. The latter were found to be approximately 10% smaller than those required by the wrought commercial tubes and easily included in a hybrid additive manufacturing commercial system.

Code availability Not applicable.

Author contribution Pragana JPM: Conceptualization, methodology, numerical modelling, experimentation, writing—editing. Bragança IMF: Conceptualization, investigation, methodology, visualization. Silva CMA: Conceptualization, investigation, methodology, visualization, supervision. Martins PAF: Conceptualization, funding acquisition, methodology, numerical modelling, supervision, writing—original draft.

Funding The authors would like to acknowledge the support provided by Fundação para a Ciência e a Tecnologia of Portugal and IDMEC under LAETA- UIDB/50022/2020.

Data availability Authors confirm that the data and material supporting the findings of this work are available within the article.

Declarations

Ethics approval The article follows the guidelines of the Committee on Publication Ethics (COPE) and involves no studies on human or animal subjects.

Consent to participate Not applicable.

Consent for publication Not applicable.

Competing interests The authors declare no competing interests.

References

1. Jiang J, Xu X, Xiong Y, Tang Y, Dong G, Kim S (2020) A novel strategy for multi-part production in additive manufacturing. Int J Adv Manuf Technol 109:1237–1248. https://doi.org/10.1007/s00170-020-05734-8
2. Daniyan I, Mpofu K, Daniyan L, Fameso F, Oyesola M (2020) Computer aided simulation and performance evaluation of additive manufacturing technology for component parts manufacturing. Int J Adv Manuf Technol 107:4517–4530. https://doi.org/10.1007/s00170-020-05340-8
3. Lu X, Zhou YF, Xing XL, Shao LY, Yang QX, Gao SY (2017) Open-source wire and arc additive manufacturing system: formability, microstructures, and mechanical properties. Int J Adv Manuf Technol 93:2145–2154. https://doi.org/10.1007/s00170-017-0636-z
4. Pragana JP, Pombinha P, Duarte VR, Rodrigues TA, Oliveira JP, Bragança IM, Santos TG, Miranda RM, Coutinho L, Silva CM (2020) Influence of processing parameters on the density of 316L stainless steel parts manufactured through laser powder bed fusion Proceedings of the Institution of Mechanical Engineers, Part B. J Eng Manuf 234:1246–1257. https://doi.org/10.1177/0954405420911768
5. Murr LE, Martinez E, Amato KN, Gaytan SM, Hernandez J, Ramirez DA, Shindo PW, Medina F, Wicker RB (2012) Fabrication of metal and alloy components by additive manufacturing: examples of 3D materials science. Journal of Materials Research and technology 1:42–54. https://doi.org/10.1016/S2238-7854(12)70009-1
6. DebRoy T, Wei HL, Zuback JS, Mukherjee T, Elmer JW, Milewski JO, Beese AM, Wilson-Heid A, De A, Zhang W (2018) Additive manufacturing of metallic components–process, structure and properties. Prog Mater Sci 92:112–224. https://doi.org/10.1016/j.pmatsci.2017.10.001
7. Ford S, Despeisse M (2016) Additive manufacturing and sustainability: an exploratory study of the advantages and challenges. J Clean Prod 137:1573–1587. https://doi.org/10.1016/j.jclepro.2016.04.150
8. Lefky CS, Zucker B, Wright D, Nassar AR, Simpson TW, Hildreth OJ (2017) Dissolvable supports in powder bed fusion-printed stainless steel. 3D Printing and Additive Manufacturing 4:3–11. https://doi.org/10.1089/3dp.2016.0043
9. Ding Y, Dwivedi R, Kovacevic R (2017) Process planning for 8-axis robotized laser-based direct metal deposition system: a case on building revolved part. Robot Comput Integr Manuf 44:67–76. https://doi.org/10.1016/j.rcim.2016.08.008
10. Yuan L, Pan Z, Ding D, He F, van Duin S, Li H, Li W (2020) Investigation of humping phenomenon for the multi-directional robotic wire and arc additive manufacturing. Robot Comput Integr Manuf 63:101916. https://doi.org/10.1016/j.rcim.2019.101916
11. Kazanas P, Deherkar P, Almeida P, Lockett H, Williams S (2012) Fabrication of geometrical features using wire and arc additive manufacture. Proceedings of the Institution of Mechanical Engineers. Part B: Journal of Engineering Manufacture 226:1042–1051. https://doi.org/10.1177/0954405412437126
12. Yoon HS, Lee JY, Kim HS, Kim MS, Kim ES, Shin YJ, Chu WS, Ahn SH (2014) A comparison of energy consumption in bulk forming, subtractive, and additive processes: review and case study. International Journal of Precision Engineering and Manufacturing-Green Technology 1:261–279. https://doi.org/10.1007/s40684-014-0033-0
13. Seow CE, Coules HE, Wu G, Khan RH, Xu X, Williams S (2019) Wire arc additively manufactured Inconel 718: effect of post-deposition heat treatments on microstructure and tensile properties. Mater Des 183:108157. https://doi.org/10.1016/j.matdes.2019.108157
14. Woodcock J (2014) Euromold roundup - bigger, bolder, busier. TCT. http://www.tctmagazine.com/blogs/jwblog/euromold-roundup-2013/. Accessed 1 August 2020
15. Merklein M, Junker D, Schaub A, Neubauer F (2016) Hybrid additive manufacturing technologies–an analysis regarding potentials and applications. Phys Procedia 83:549–559. https://doi.org/10.1016/j.phpro.2016.08.057
16. Silva CMA, Bragança IMF, Cabrita A, Quintino L, Martins PAF (2017) Formability of a wire arc deposited aluminium alloy. J Braz Soc Mech Sci Eng 39:4059–4068. https://doi.org/10.1007/s40430-017-0864-z
17. Pragana JPM, Cristino VAM, Bragança IMF, Silva CMA, Martins PAF (2020) Integration of forming operations on hybrid additive manufacturing systems based on fusion welding. International Journal of Precision Engineering and Manufacturing-Green Technology 7:595–607. https://doi.org/10.1007/s40684-019-00152-y
18. Schulte R, Papke T, Lechner M, Merklein M (2020) Additive manufacturing of tailored blank for sheet-bulk metal forming processes. IOP Conf Ser Mater Sci Eng 967:12034
19. Rosenthal S, Platt S, Jager RH, Gies S, Kleszczynski S, Tekkaya AE, Witt G (2019) Forming properties of additively manufactured monolithic Hastelloy X sheets. Mater Sci Eng A 753:300–316. https://doi.org/10.1016/j.msea.2019.03.035
20. Ambrogio G, Gagliardi F, Muzzupappa M, Filice L (2019) Additive-incremental forming hybrid manufacturing technique to improve customised part performance. J Manuf Process 37:386–391. https://doi.org/10.1016/j.jmapro.2018.12.008
21. Baptista RJS, Pragana JPM, Bragança IMF, Silva CMA, Alves LM, Martins PAF (2020) Joining aluminium profiles to composite sheets by additive manufacturing and forming. J Mater Process Technol 279:116587. https://doi.org/10.1016/j.jmatprotec.2019.116587
22. Pragana JPM, Rosenthal S, Alexandrino P, Araújo A, Bragança IMF, Silva CMA, Leitão PJ, Tekkaya AE, Martins PAF (2021) Coin minting by additive manufacturing and forming. Proc Inst Mech Eng B J Eng Manuf 235:819–828. https://doi.org/10.1177/0954405420971128
23. Pragana JP, Rosenthal S, Bragança IM, Silva C, Tekkaya AE, Martins PA (2020) Hybrid additive manufacturing of collector coins. Journal of Manufacturing and Materials Processing 4:115. https://doi.org/10.3390/jmmp4040115

24. Bambach M, Sizova I, Sydow B, Hemes S, Meiners F (2020) Hybrid manufacturing of components from Ti-6Al-4V by metal forming and wire-arc additive manufacturing. J Mater Process Technol 282:116689. https://doi.org/10.1016/j.jmatprotec.2020.116689
25. Pragana JPM, Sampaio RFV, Bragança IMF, Silva CMA, Martins PAF (2021) Hybrid metal additive manufacturing: a state–of–the-art review. Advances in Industrial and Manufacturing Engineering 2:100032. https://doi.org/10.1016/j.aime.2021.100032
26. Almeida BPP, Alves ML, Rosa PAR, Brito AG, Martins PAF (2006) Expansion and reduction of thin-walled tubes using a die: experimental and theoretical investigation. Int J Mach Tools Manuf 46:1643–1652. https://doi.org/10.1016/j.ijmachtools.2005.08.018
27. Pragana JPM, Bragança IMF, Silva CMA, Martins PAF. 2021. Revisiting the ring hoop test in additively manufactured metal tubes. Journal of Strain Analysis in Engineering Design (submitted).
28. ASTM (2016) E8/E8M. Standard test methods for tension testing of metallic materials, ASTM International, West Conshohocken, USA
29. ASTM (2000) D2290-00. Standard test method for apparent hoop tensile strength of plastic or reinforced plastic pipe by split disk method, ASTM International, West Conshohocken, USA
30. Nielsen CV, Martins PAF (2021) Finite element simulation: a user's perspective, In: Metal forming: formability, simulation and tool design. Academic Press, London. https://doi.org/10.1016/B978-0-323-85255-5.00011-X
31. Hill R (1948) A theory of yielding and plastic flow of anisotropic metals. Proceedings of the Royal Society of London (Series A). 193:281–297
32. McClintock FA (1968) A criterion for ductile fracture by the growth of holes. Journal of Applied Mechanics – Transactions ASME 35:363–371
33. Cristino VA, Magrinho JP, Centeno G, Silva MB, Martins PAF (2019) A digital image correlation based methodology to characterize formability in tube forming. The Journal of Strain Analysis for Engineering Design 54:139–148. https://doi.org/10.1177/0309324718823629
34. Martins PAF, Bay N, Tekkaya AE, Atkins AG (2014) Characterization of fracture loci in metal forming. Int J Mech Sci 83:112–123. https://doi.org/10.1016/j.ijmecsci.2014.04.003